J. Plasma Physics (1999), *vol.* 61, *part* 5, *pp.* 701–722. Printed in the United Kingdom
© 1999 Cambridge University Press

Unstructured adaptive grid and grid-free methods for edge plasma fluid simulations

O. V. BATISHCHEV,[1–4] A. A. BATISHCHEVA[1] and A. S. KHOLODOV[3]

[1] Massachusetts Institute of Technology Plasma Science and Fusion Center, Cambridge, MA 02139, USA

[2] Lodestar Research Corporation, Boulder, CO 80301, USA

[3] Moscow Institute of Physics and Technology, Dolgoprudny 141700, Russia

[4] Keldysh Institute for Applied Mathematics, Moscow 125047, Russia

(Received 25 June 1998 and in revised form 19 February 1999)

Fluid modelling of an edge plasma is usually performed using a finite-difference scheme on a fixed structured grid. However, both experimental measurement and numerical simulation show the presence of front-like regions characterized by sharp variations of the main plasma parameters such as temperature and radiation power. This is caused in part (i) by strong nonlinearities in the fluid equation coefficients due to abrupt changes of various plasma reaction rates as a function of temperature and (ii) by high anisotropy of the plasma transport along and across magnetic field lines. Manual mesh adoption is usually applied to allow better resolution of the regions with sharp gradients. However, such an approach is very time-consuming and limited. To overcome this problem, we propose to use adaptive unstructured meshes constructed with a new quasi-one-dimensional adaption algorithm. This approach is fast and conservative because we use a new finite-volume scheme. The price of adaptation is high, because numerical algorithms became much more complicated. To avoid unwanted complexity, we suggest an alternative use of a grid-free method, which requires no connectivity of arbitrarily placed vertices. To benchmark the methods and codes in two dimensions, we find analytical and semi-analytical solutions of the nonlinear diffusion–radiation equation, which may have sharp fronts, unconnected boundaries and bifurcated solutions. We use these solutions to study the efficiency of the proposed numerical algorithms.

1. Introduction

Numerical simulation of edge plasmas is an extremely challenging computational problem. The primary reasons for this arise from the wide ranges of time scales and space scales that are intrinsic to edge plasmas. Another important source of difficulties is the strong nonlinearity of the fluid equations due to the abrupt thresholds in the atomic physics rate constants and the huge anisotropy of plasma transport coefficients along and across the magnetic field. The predictive simulation of tokamak scrape-off layer (SOL) plasmas in the promising detached regimes requires the resolution of sharp fronts, associated with essential radiation, ionization and recombination processes. These fronts may have complicated spatial structures, and

https://doi.org/10.1017/S0022377899007679 Published online by Cambridge University Press

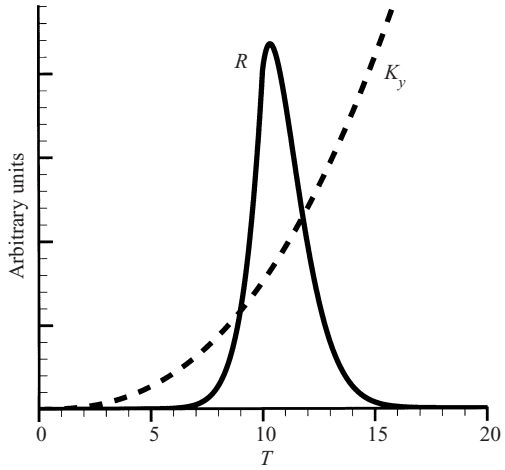


Figure 1. The carbon-like radiation function $R(T)$ and classical parallel heat conduction coefficient K_y are sharply varying functions of the plasma temperature T.

are characterized by short millimetre scale lengths, provided the machine dimensions are of the order of metres. The location of these fronts is a priori unknown. However, the location and parameters of these fronts are crucial for the accurate modelling of edge plasmas that is required for the design of future fusion reactors and for the interpretation of experimental results from research tokamaks.

Fine spatial structure requires enhanced resolution in both angular and radial directions. For this reason, the usual structured meshes are very limited. One cannot refine such a mesh locally by adding a single node, because at least one row or one column must be added at a time. To keep the simulations on a reasonable time frame, we have to keep the number of nodes limited. Thus edge plasma modelling is ideally suited to unstructured adaptive grid algorithms. Of course, we have to keep the separation of grid vertices inversely proportional to the local plasma gradients. Another interesting feature of SOL plasmas is that several stable solutions may be allowed for the same input conditions (Wising et al. 1996).

Several attempts have been made previously to develop static unstructured meshes and algorithms for fluid codes (Zanino 1996; Zanino and Subba 1998) and to simulate SOL plasmas under realistic conditions (Marchand et al. 1998). Unlike the pure finite-element methods used before, our approach is conservative. However, it differs from the usual finite-volume methods (Baliga and Patankar 1983), since (i) it does not require the creation of Dirichlet cells to achieve conservation, and (ii) cells are mandatorily aligned with the local magnetic field.

To illustrate the difficulty of the fluid modelling of edge plasmas, we have focused on a single two-dimensional non-stationary nonlinear heat conduction–radiation equation for the plasma temperature T, with strongly anisotropic nonlinear heat conductivities, and with a nonlinear radiation term R:

$$\frac{\partial T}{\partial t} - \nabla_x K_x \nabla_x T - \nabla_y K_y \nabla_y T = -R(T, x, y). \tag{1}$$

Here x and y are directions perpendicular and parallel to the magnetic field respectively. This equation has no analytical solution for a carbon-like radiation function $R(T)$ (which is shown in Fig. 1, along with a nonlinear $K_y \propto T^{2.5}$; K_x was fixed

https://doi.org/10.1017/S0022377899007679 Published online by Cambridge University Press

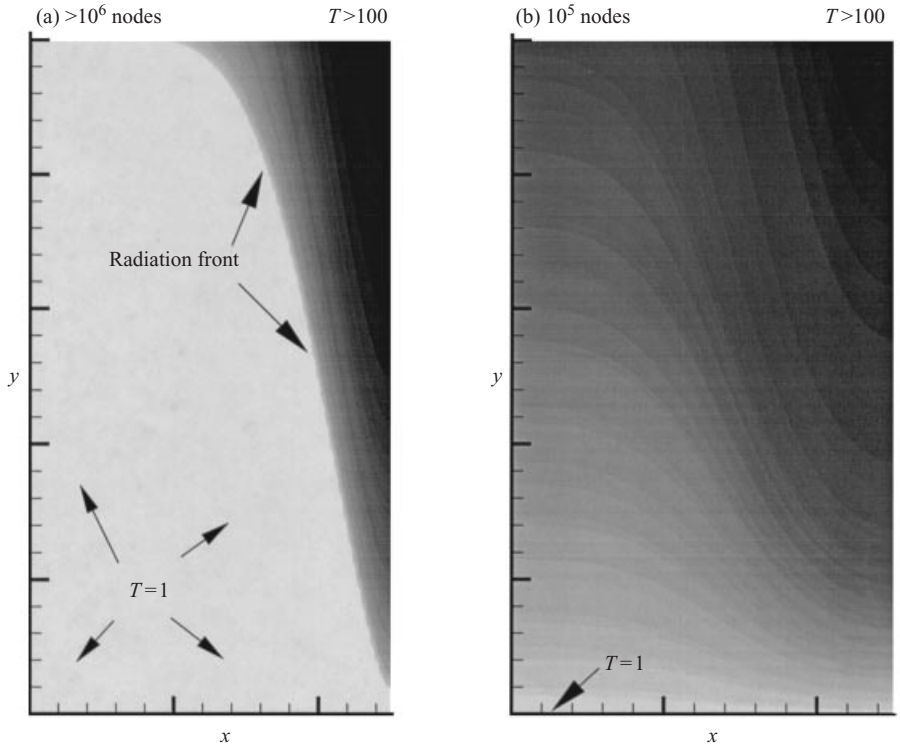


Figure 2. The position of the radiative front is very sensitive to mesh refinement near the bifurcation threshold.

here):

$$R(T) = R_0 c(T) \times \begin{cases} e^{-w} \dfrac{(T/T_0)^3}{T^2 + g^2(T_0 - T)} & (T < T_0), \\ (2 - e^{-w}) \dfrac{T_0^3}{T^5} & (T \geqslant T_0), \end{cases} \tag{2}$$

where

$$w = \left| \frac{T_0 - T}{g} \right|, \qquad c(T) = 1 + a e^{-w^2/b};$$

R_0, T_0, a, b and g are constants. However, it was shown that (1) with R given by (2) can exhibit a bifurcation of its solutions (Krasheninnikov 1997). It was also determined by the modelling that around the bifurcation threshold, the numerical solution of (1) and (2) is extremely sensitive to the spatial resolution. Figures 2(a,b) represent fully converged solutions of (1) for a particular set of parameters on a structured non-uniform grid. The only difference between these solutions is that one (b) was obtained on a fine mesh with 10^5 nodes, and the other (a) on a 10 times finer mesh with a total of more than 10^6 nodes. All other numerical parameters and boundary conditions were the same. Such behaviour is quite typical, as will be shown later for the one-dimensional heat conduction equation. However, in reality, R may have several maxima. Thus there could be a few regions with sensitive bifurcated solutions.

From a numerical point of view, to reliably prove our methods and code accu-

https://doi.org/10.1017/S0022377899007679 Published online by Cambridge University Press

racy, we have to have test problems with exact analytical or easy-to-find numerical solutions of (1), which in addition exhibit some of the listed SOL plasma properties.

The structure of this paper is as follows. In Sec. 2 we describe the test problems for a two-dimensional nonlinear diffusion–radiation equation, and discuss the numerical results obtained for each of them using our adaptive approach. The main details of the new adaptive grid method are discussed in Sec. 3. The grid-free method is introduced in Sec. 4. The results of modelling of the two test problems with the grid-free method are presented at the end of Sec. 4. Our main results are summarized in Sec. 5.

2. Model analytical problems

We construct test problems to exhibit the main features of the SOL plasma in tokamaks. The latter may include (i) a few orders of magnitude variation of the temperature along the magnetic field, (ii) the presence of several unconnected boundaries, and, possibly, (iii) allowing bifurcated solutions. Furthermore, we want the solutions to contain controllable sharp gradients (fronts) for benchmarking purposes. Below, we specify three such problems for which analytical or semi-analytical solutions of the nonlinear (1) have been found.

2.1. Two unconnected boundaries

Axisymmetric models of the tokamak SOL plasma usually have two unconnected boundaries. The first is an internal boundary, which corresponds to a core plasma, with high temperature T_C^0. The second boundary is external, and corresponds to a cold edge, located at the open magnetic lines, with the plasma at a much lower temperature $T_E^0 \ll T_C^0$.

It is possible in some cases (e.g for $\beta = \alpha$, see below) to find an analytical solution of (1) that mimics this feature. This solution is characterized by sharp, but still controllable, gradients. The nine-parameter $\{\sigma, \alpha, a, b, c, x_c, y_c, T_C^0, T_E^0\}$ family of positive smooth stationary analytical solutions of (1) is given by

$$T_b(x,y) = \begin{cases} [(\alpha+1)\, T_C\, (e^{-\delta} + T_E)]^{1/(\alpha+1)} & (r > c > a), \\ [(\alpha+1)\, T_C\, (2 - e^{-\delta} + T_E)]^{1/(\alpha+1)} & (r \leqslant c < b) \end{cases} \tag{3}$$

in a ring $0 < a \leqslant r \equiv [(x-x_c)^2 + (y-y_c)^2]^{1/2} \leqslant b$ with nonlinear heat conduction coefficients taken in the usual fixed-power form as $K_x = T^\alpha$ and $K_y = T^\beta$, and with a nonlinear term on the right-hand side of the form

$$R(T) = \pm \frac{4T_0\delta^{0.5}}{\sigma^2} \left(4\delta - \frac{\Delta}{\Delta + c} - 3\right) e^{-\delta}, \tag{4}$$

where $\Delta = \sigma\delta^{0.25}$, and $\delta(T)$ is defined by

$$e^{-\delta} = \begin{cases} \dfrac{T^{\alpha+1}}{(\alpha+1)T_C} - T_E & (r > c), \\ T_E + 2 - \dfrac{T^{\alpha+1}}{(\alpha+1)T_C} & (r \leqslant c). \end{cases} \tag{5}$$

The imposed boundary conditions preserve constant T_C^0 and T_E^0 as

$$\begin{aligned} T_C^0 \equiv T(r=a) &= [2(\alpha+1)(T_E+2)T_C]^{1/(\alpha+1)} \\ &\gg [(\alpha+1)T_E T_C]^{1/(\alpha+1)} = T(r=b) \equiv T_E^0. \end{aligned} \tag{6}$$

https://doi.org/10.1017/S0022377899007679 Published online by Cambridge University Press

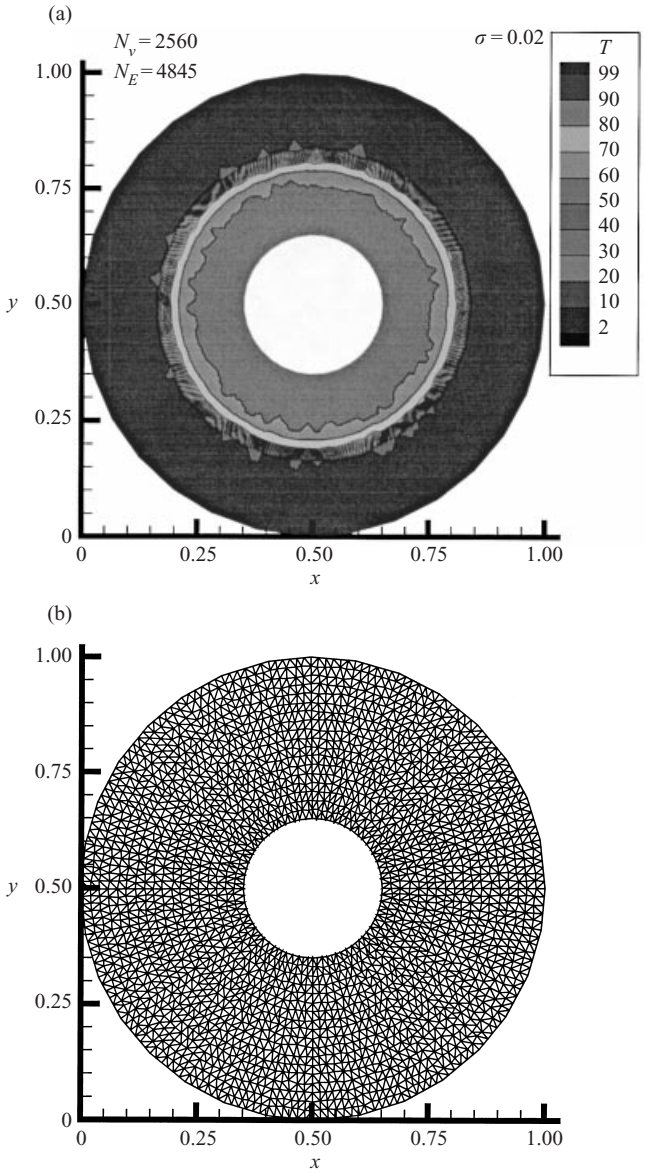


Figure 3. (a) Stationary solution of the first test problem on a coarse initial mesh, shown in (b).

The adaption of an adjustable grid to a particular stationary solution of (1) with the key parameters $\sigma = 0.02$, $b = 0.5$, $a = 0.15$, $T_C^0 = 100$, $T_E^0 = 1$, $x_c = y_c = 0.5$, $\alpha = 2.5$ and $c = 0.3$ is shown in Figs 3 and 4. In Fig. 3(b) we show the initial unstructured triangular mesh. It has nearly uniform resolution in both x and y directions throughout the domain. The total number of triangular elements, N_E, and the total number of vertices, N_V, are about 5000 and 2500 respectively. A numerical solution of (1), T_1, obtained with this initial mesh, is shown in Fig. 3(a).

https://doi.org/10.1017/S0022377899007679 Published online by Cambridge University Press

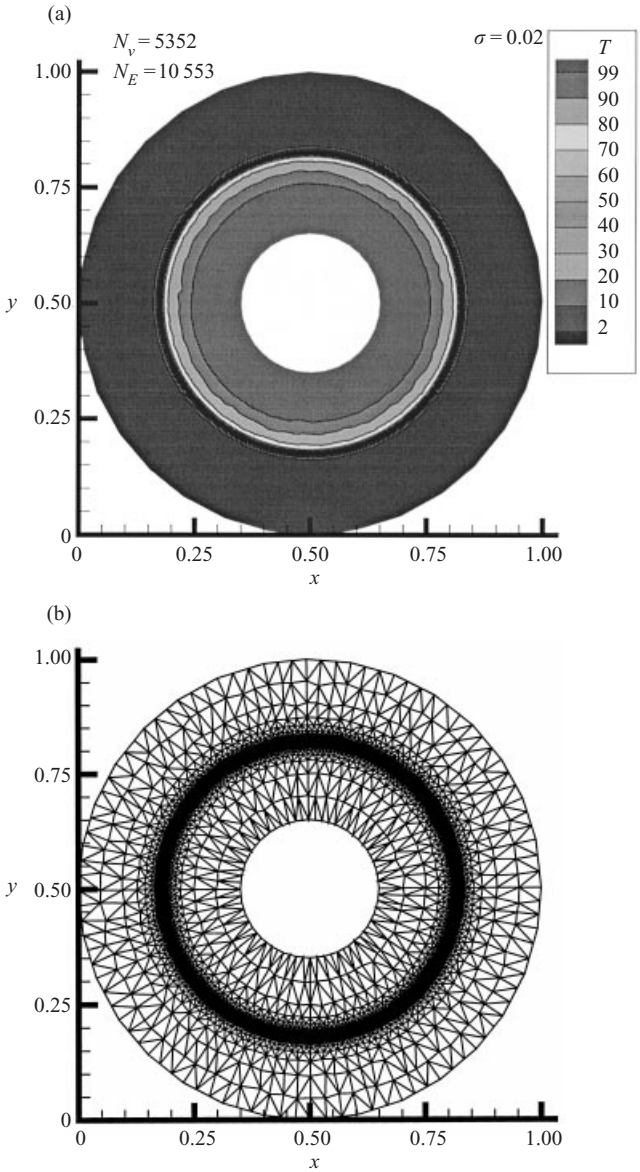


Figure 4. (a) Steady-state solution of the same problem as in Fig. 3, but on the adapted fine mesh, shown in (b).

The relative accuracy

$$\varepsilon = \max_{i=1,\ldots,N_V} \left| 1 - \frac{T_1^i}{T_b(x_i, y_i)} \right|,$$

is about 1, where (x_i, y_i) are the coordinates of the ith vertex. After the solution was obtained, the grid was allowed to accommodate to the calculated gradients in both directions. Next, a new stationary numerical solution T_2 was calculated, and the iterative procedure was repeated a few times. The adaptive mesh obtained

https://doi.org/10.1017/S0022377899007679 Published online by Cambridge University Press

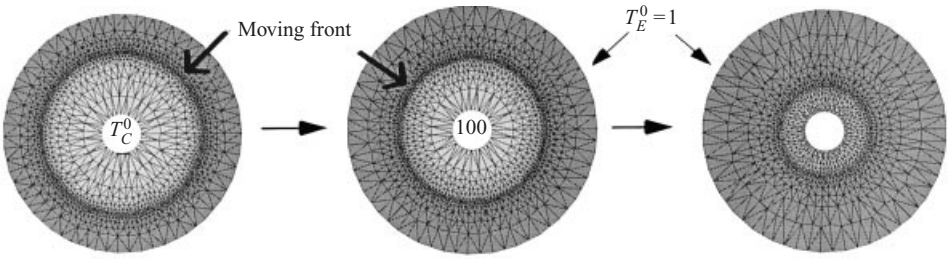


Figure 5. Automatic mesh adaption to the moving circular front.

after 10 iterations is shown in Fig. 4(b). The total number of vertices is about 5000. We note that the ratio of the number of triangles ($N_E \approx 10^4$) to the number of vertices is 1.97. This indicates that the adapted mesh is close to an ideal one, which asymptotically, as $N \to \infty$, has a N_E/N_V ratio of 2. The 'adapted' numerical solution T_{10} is shown in Fig. 4(a), and is characterized by a much better relative error ε, of the order of 10^{-3}, because of the much finer mesh near the step in T.

Next, an analytical non-stationary solution of (1) (where c may vary with time) was used to study the efficiency of the grid adaption algorithm. Figure 5 shows the consecutive patterns of mesh automatic adaptation to a moving temperature gradient front with two parameters modified ($\sigma = 0.05$ and $a = 0.08$; the other parameters are the same), which was shifting axisymmetrically towards the axis. The total number of vertices in this run was around 6000 and remained almost constant, while a three-digit agreement of the numerical solution with the analytical solution was preserved. We note that the solution given by (5) with Dirichlet boundary conditions may be used as a test not only in a circular region, but also in an arbitrarily shaped domain, with any number of unconnected boundaries (for example as shown in Sec. 4).

2.2. V-shaped fronts

As has previously been mentioned, the radiation fronts might have arbitrary shapes. In a divertor, they are usually V-shaped. For $\beta \neq \alpha$, we have found a nonlinear analytical solution of (1) that demonstrates precisely this feature in a rectangular $x \times y \in [0, 1] \times [0, L_y]$ domain

$$T_V(x, y) = \begin{cases} 0.5e^{-\sigma[y_f(x)-y]^p} & (y < y_f(x)), \\ 1 - 0.5e^{-\sigma[y-y_f(x)]^p} & (y \geqslant y_f(x)), \end{cases} \tag{7}$$

with a controllable 'parabolic' front

$$y_f = y_v + r \mid x - x_v \mid^s . \tag{8}$$

The solution depends on six free parameters $\{\sigma, p, x_v, y_v, r, s\}$. The specially constructed radiation sink term R reads as

$$R(T, x, y) = \begin{cases} T^{\alpha+1}(\alpha a^2 + b) + T^{\beta+1}(\beta c^2 + d) & (y < y_f(x)), \\ T^{\alpha-1}[\alpha(T-1)^2 a^2 + T(T-1)b] & \\ \quad + T^{\beta-1}[\beta(T-1)^2 c^2 + T(T-1)d] & (y \geqslant y_f(x)). \end{cases} \tag{9}$$

https://doi.org/10.1017/S0022377899007679 Published online by Cambridge University Press

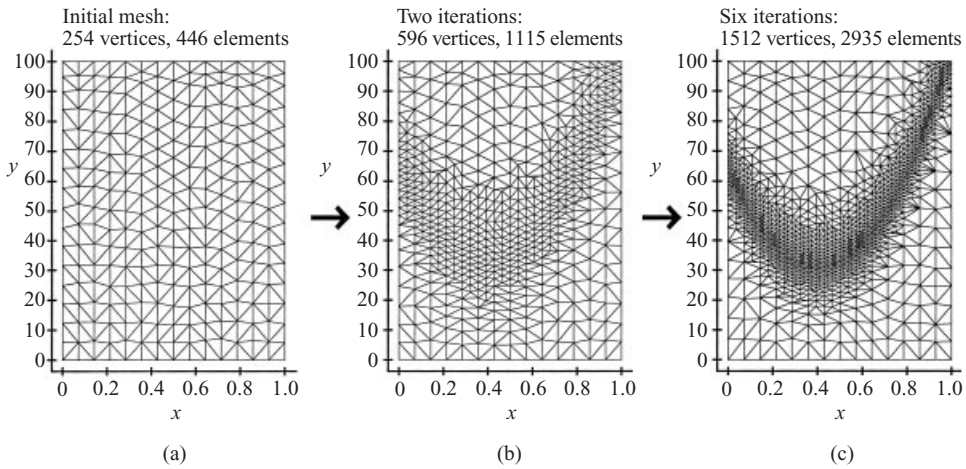


Figure 6. Field-aligned unstructured triangular grid adaption to a V-shaped stationary front: (a) initial mesh; (b) grid after two iterations; (c) grid after six iterations.

The coefficients c, d, a and b are defined as

$$c(x,y) = \sigma p(y_f - y)^{p-1}, \tag{10}$$

$$d(x,y) = \sigma p(y_f - y)^{p-2}[\sigma p(y_f - y)^p + p - 1], \tag{11}$$

$$a(x,y) = -\sigma p(y_f - y)^{p-1}\delta, \tag{12}$$

$$b(x,y) = \sigma p(y_f - y)^{p-2}\{[\sigma p(y_f - y)^p - p + 1]\delta^2 - (y_f - y)\Delta\}, \tag{13}$$

in terms of

$$\delta = rs(x - x_v)^{s-1}, \tag{14}$$

$$\Delta = rs(s-1)(x - x_v)^{s-2}, \tag{15}$$

where we have additionally assumed that $p \geqslant 2$ and $s \geqslant 2$.

Two examples of adaptive mesh application to the second test problem are shown in Figs 6 and 7. Figure 6 illustrates the mesh adaption for a fixed parameters $\sigma = 0.05$, $p = s = 2$, $x_v = 0.4$, $y_v = 30$, $r = 200$, $L_y = 100$, $\alpha = 2.5$ and $\beta = 1$. We present here the initial mesh, and the grid after two and six iterative adjustments to the stationary solution. We have additionally demanded that each triangular element have one side parallel to the magnetic field, which is strictly vertical in this case. However, one can see from Fig. 6 that the constraint of the alignment of the elements with the magnetic field direction is in conflict with smooth variation of the mesh sizes (it doubles at certain locations).

The grid adaptation saturates when the temperature difference between each pair of adjacent vertices becomes smaller than some prescribed value:

$$|T_i - T_j| < \epsilon \max\{1, \min\{T_i, T_j\}\}$$

(we have used $\epsilon = 0.04$). Figures 7(a–d) show that final mesh refinement depends on the solution sharpness, which is determined by a variable parameter σ, provided that the rest of the parameters are fixed ($x_v = 0.45$, $y_v = 20$, $r = 400$; others are as before). Figures 7(a) and (c) represent the numerical solutions, while (b) and (d) show the 'final' meshes for $\sigma = 0.03$ and $\sigma = 0.12$ respectively. The initial grid was the same. One can see that the number of vertices has increased four times,

https://doi.org/10.1017/S0022377899007679 Published online by Cambridge University Press

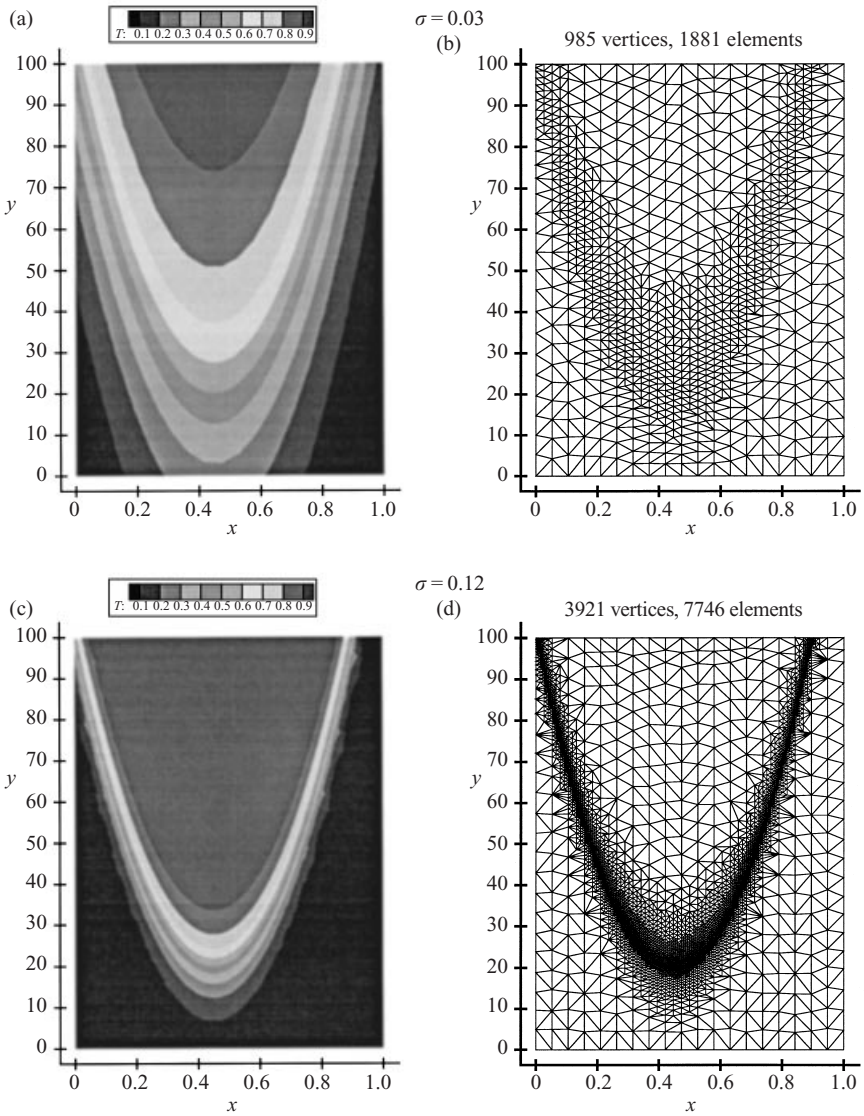


Figure 7. The final adaptive mesh depends on the local gradients. The sharper the gradients, the more magnetic line subdivisions will be required before the algorithm saturates.

while the gradient has become ten times larger. Thus we can conclude that the unstructured mesh allows us to have 25 times fewer vertices to achieve the same accuracy, compared with the common non-uniform structured rectangular grid.

2.3. Bifurcated solutions

In this subsection we introduce bifurcated solutions of the steady-state one-dimensional non-linear reduction of the heat conduction–radiation equation. The equation follows trivially from (1) on assuming that $\partial/\partial t = \partial/\partial x \equiv 0$:

$$\frac{\partial}{\partial y}\left[K_y(T)\frac{\partial T}{\partial y}\right] = R(T). \tag{16}$$

https://doi.org/10.1017/S0022377899007679 Published online by Cambridge University Press

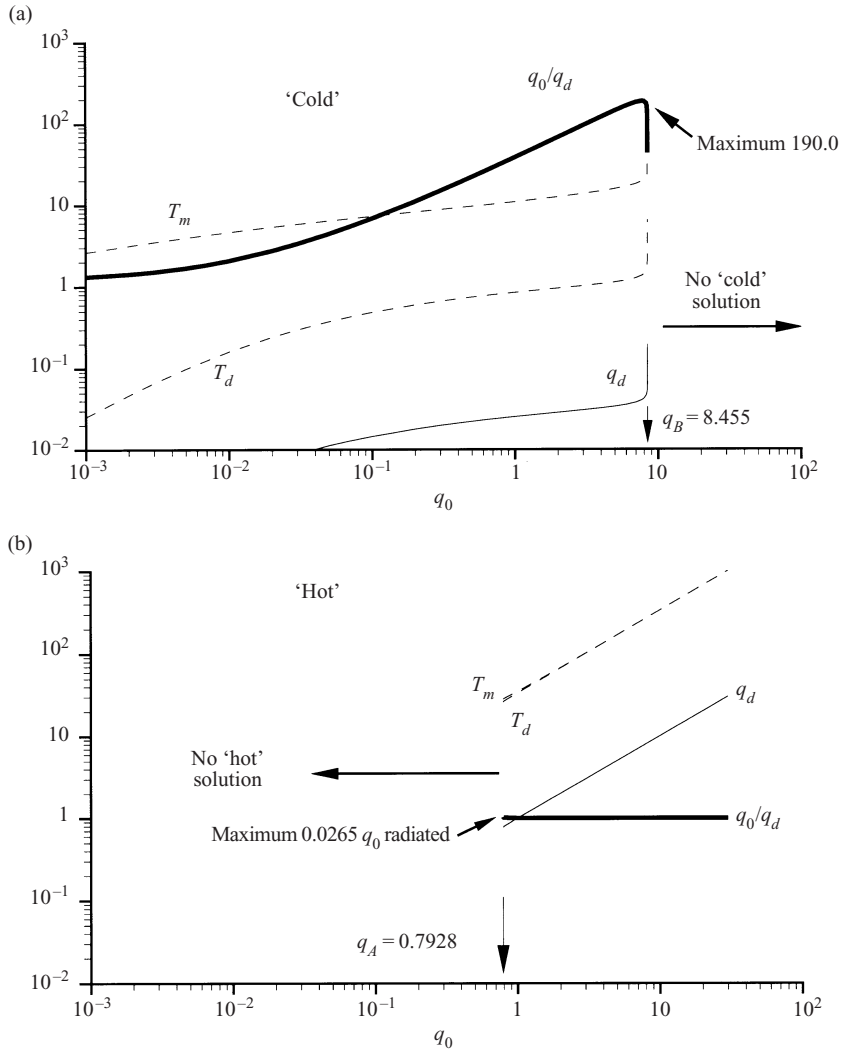


Figure 8. One-dimensional bifurcation study. Parameters of (a) the cold solution and (b) the branches of the solution. There is a broad region of q_0 where two solutions coexist.

This equation may be reduced to a full integral by (i) multiplying by $q_y = K_y \partial T/\partial y$ and by (ii) switching to a new independent variable T instead of y, resulting in

$$q_y^2(y) = q_0^2 - \int_{T(y)}^{T(L_y)} 2K_y(T')R(T')\,dT', \tag{17}$$

where q_0 is the incoming heat flux at the $y = L_y$ end of the interval, which serves as a first boundary condition. The second boundary condition at $y = 0$ is 'responsible' for the bifurcation, because it was chosen to be dependent on the solution as

$$q_y = \gamma T, \qquad y = 0. \tag{18}$$

https://doi.org/10.1017/S0022377899007679 Published online by Cambridge University Press

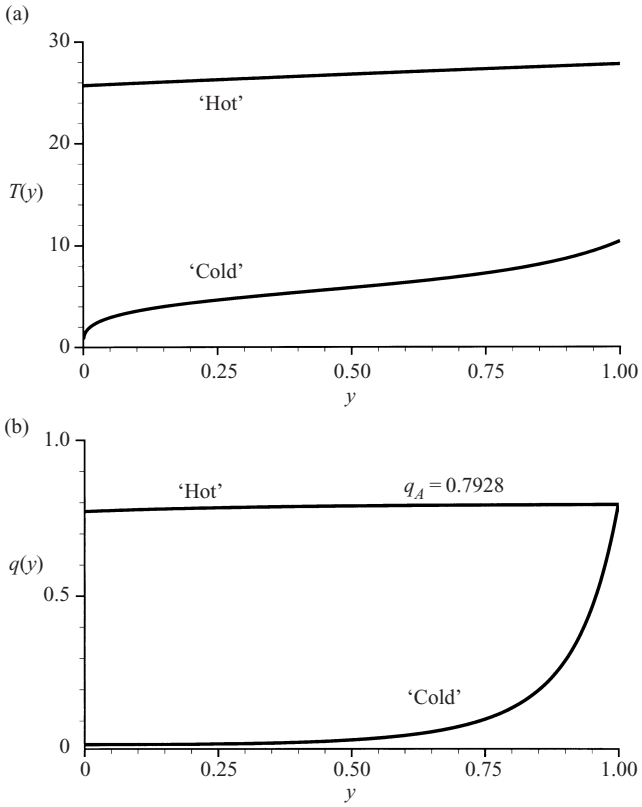


Figure 9. (a) Hot and cold solutions $T(y)$ of the one-dimensional diffusion–radiation equation. (b) The corresponding heat flux profiles $q(y)$. q_0 is slightly above the lower threshold q_A.

If the energy transmission factor γ is small, we may have two different solutions of the equation, provided the incoming heat flux rises to

$$q_0 \approx \left[\int_0^\infty 2K_y(T')R(T')\,dT'\right]^{1/2}.$$

The first solution corresponds to a hot plasma profile, with no radiated power. Thus the heat flux is almost constant, $q_y \approx q_0$, as well as the temperature, $T \approx q_0/\gamma$. The second solution corresponds to a cold branch with almost all heat energy radiated, and thus low temperature T_D at $x = 0$, compared with the temperature T_m at $x = L_y$. If the radiation function $R(T)$ is localized in T (in other words, if there is a T^* such that $[\int_0^{T^*} 2K_y(T')R(T')\,dT']^{1/2} \approx q_0$) then there could be an interval of q_0 values where two solutions coexist.

To illustrate this feature, we consider the following simple model problem in the interval $y \in [0, 1]$. We take the source term in the form

$$R(T) = C\frac{T}{T_0}\exp\left[-\left(\frac{T - T_0}{\sigma}\right)^2\right]. \tag{19}$$

Results for a particular set of coefficients $C = 50$, $T_0 = 15$, $\sigma = 4$, $\gamma = 0.03$ and $K_y = 10^{-4}T^{2.5}$ are presented in Figs 8–10. In Fig. 8(a), the key parameters of the cold solution, which exists for a limited interval of $q_0 \in [0, q_B]$, are presented. The

https://doi.org/10.1017/S0022377899007679 Published online by Cambridge University Press

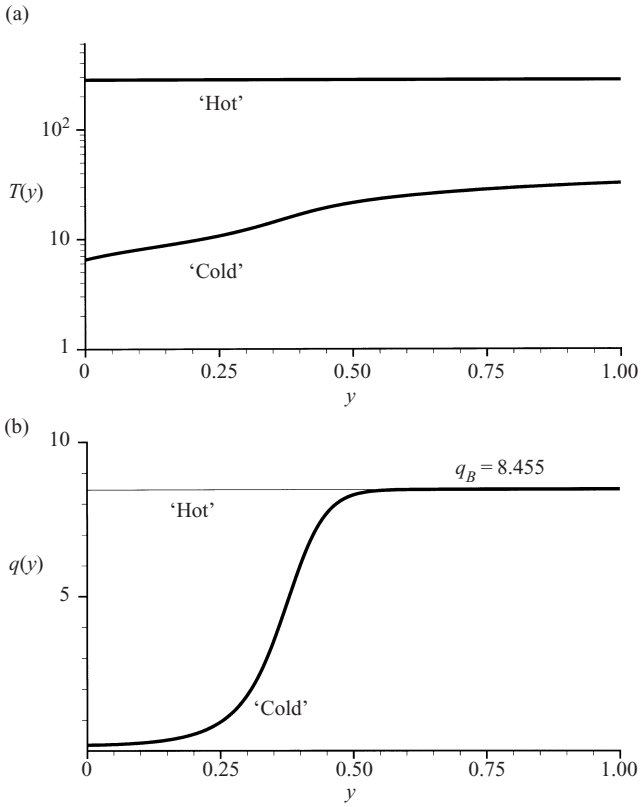


Figure 10. Same as Fig. 9, but for an incoming heat flux q_0 slightly lower than the upper threshold q_B.

'hot' solution, in contrast, exists in the unlimited interval $[q_A, \infty]$, as can be seen in Fig. 8(b). Thus there is a broad interval $q_0 \in [q_A, q_B] \approx [0.7928\ldots, 8.455\ldots]$ where the bifurcated solutions occur.

Both cold and hot coexisting solutions are shown in Figs 9(a) and 10(a) near the lower and upper bifurcation thresholds respectively. The corresponding profiles of the heat flux are shown in Figs 9(b) and 10(b).

Next, these one-dimensional solutions were used to benchmark the two-dimensional code. The sharp variation of the two-dimensional solution in a box geometry is shown in Fig. 11, where the spatial distribution of a radiation sink $R(x, y)$ is presented. As can be seen, the location of its maximum moves rapidly with small variation of q_0.

3. Adaptive grid method

We believe that our approach is novel and exhibits a composite nature. Overall, it may be called a 'finite-element–finite-volume hybrid', because it combines features of both methods. In our method, the unknowns $\{T_i^n\}$ are defined at the moving grid vertex locations, $\{x_i^n, y_i^n\}, i = N_{V_n}$. The total number of vertices, N_{V_n}, may vary from the previous iteration n to the next iteration of the mesh adaption (regriding). The triangular grid is formed using these vertices, as shown in Fig. 12. The num-

https://doi.org/10.1017/S0022377899007679 Published online by Cambridge University Press

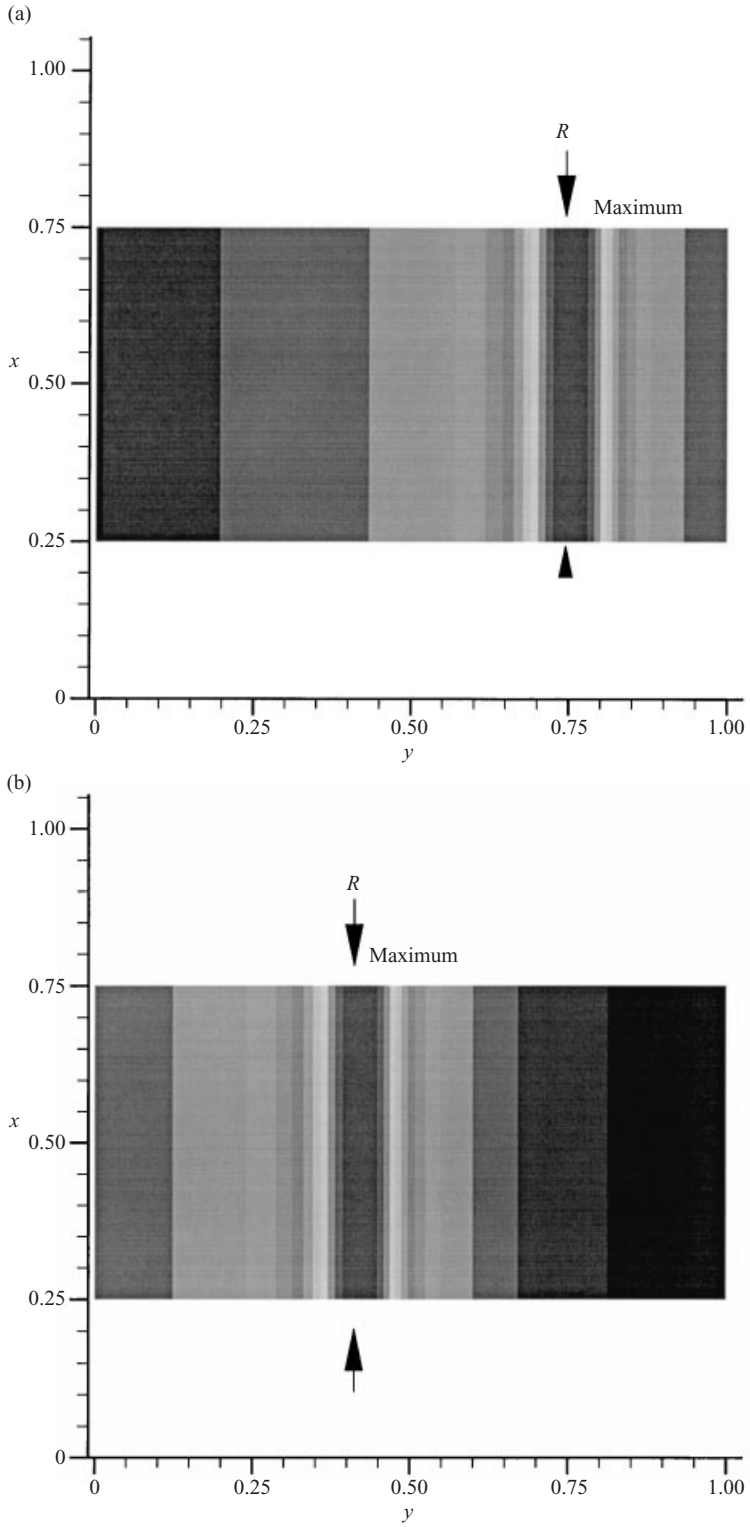


Figure 11. Illustration of a large shift in the radiation profile $R(x, t)$ with a small variation in the incoming heat flux: (a) $q_0 = 8.45$; (b) $q_0 = 8.455$.

https://doi.org/10.1017/S0022377899007679 Published online by Cambridge University Press

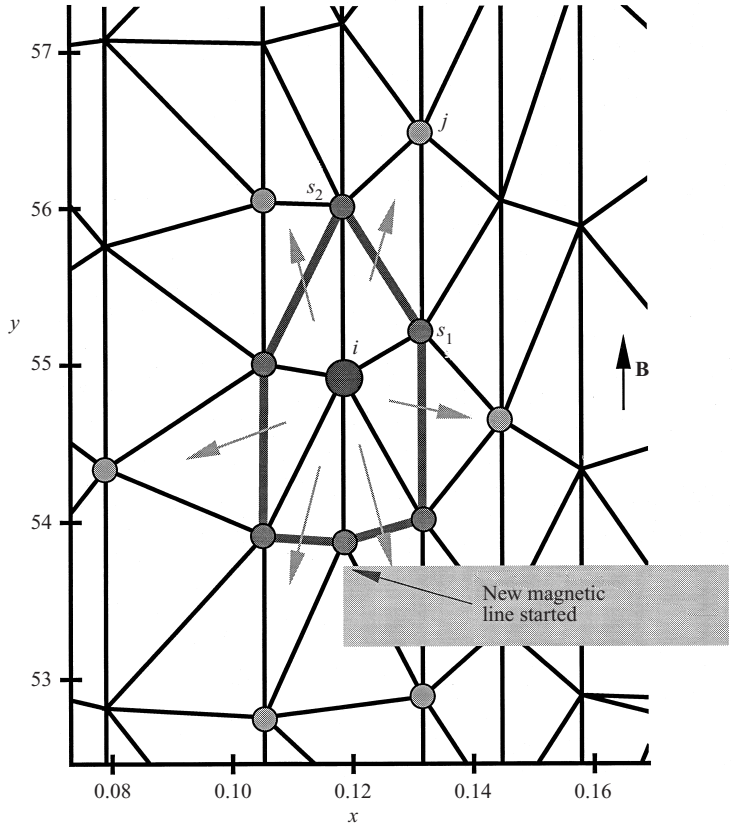


Figure 12. A fragment of an actual unstructured triangular adaptive mesh, showing the definition of cell volume, vertex dependence region, calculation of fluxes, and mesh alignment with the magnetic field B.

ber of triangular elements, $\{E_k^n\}, k = 1, \ldots, N_{E_n}$, with individual volumes $\{V_k^n\}$, is roughly twice as large as the number of vertices, $N_{E_n} \approx 2N_{V_n}$, at any iteration.

The scheme is conservative. We achieve this important feature without introducing any new grids, and without constructing Dirichlet cells, as is usually done (Baliga and Patankar 1983). Instead, we propose the following new finite-volume approach for the triangular mesh:

(i) all quantities are strictly cell-averaged, and the number of cells is equal to the number of nodes;

(ii) the ith macrocell C_i is a composition of all the triangles (one or more) that have the ith node as one of their corners:

$$C_i = \bigcup_{m=1}^{M_i} E_{k_m}, \qquad (x_i, y_i) \in E_{k_m}. \tag{20}$$

Thus the same triangular element E_k will be used in forming different cell elements, centred around each of the triangle's corners. Despite this, the conservation law may be now written in a generalized form.

First, we define the energy content of each triangular element (we leave out the

https://doi.org/10.1017/S0022377899007679 Published online by Cambridge University Press

index n below) as

$$Q_k^3 = \tfrac{1}{3} C_v V_k \sum_{i=1}^{3} T_{k_i} = C_v V_k \langle T_k \rangle, \tag{21}$$

where C_v is the specific heat and $\langle T_k \rangle = \frac{1}{3}(T_{k_1} + T_{k_2} + T_{k_3})$ is the mean temperature within the triangle.

The energy stored in each macrocell centred around node i is

$$Q_i = \tfrac{1}{3} C_v T_i \sum_{j=1}^{J_i} V_{i_j}. \tag{22}$$

Thus the total energy in the system is

$$Q_{\text{total}} = \sum_{i=1}^{N_V} Q_i = \sum_{k=1}^{N_E} Q_k^3. \tag{23}$$

The time evolution of T_i is governed (assuming no radiation, for simplicity) by the equation

$$C_v \frac{dT_i}{dt} \sum_{j=1}^{J_i} V_{i_j} = \sum_{j=1}^{j_i} q_{ji}, \tag{24}$$

where q_{ji} is the heat coming to the ith macrocell from the jth vertex through the corresponding boundary (see Fig. 12). So, the total energy content will evolve as

$$\frac{dQ_{\text{total}}}{dt} = \frac{1}{3} \sum_{i=1}^{N_V} \sum_{j=1}^{j_i} q_{ji} = \sum_{i>j} (q_{ji} + q_{ij}) + \sum_{l=1}^{L} q_{\Gamma_l}, \tag{25}$$

where q_{Γ_l} is the flux through the lth piece of the boundary.

To take the final step towards a fully conservative scheme, we have to set all fluxes through adjacent cell surfaces to be the same, namely $q_{ji} = -q_{ij}$. This is done using a continuous four-point interpolation that includes two 'exchanging' cell centres (i and j in Fig. 12) and two vertices s_1 and s_2 that form the surface:

$$f_{i-j}(x, y) = T_i + c_x^{i-j}(x - x_i) + [c_y^{i-j} - c_{xy}^{i-j}(x - x_i)](y - y_i). \tag{26}$$

This interpolation function can always be found for our mesh, and it is always symmetric, provided that $f_{i-j}(x_i, y_i) = T_i$ for the other three corners of the quadrilateral. Now, to calculate, for example, the parallel heat flux through the i–j surface, we need to calculate the integral

$$q_x^{i-j} = \int_{x_{s1}}^{x_{s2}} K_y \nabla_y f_{i-j}\, dx, \tag{27}$$

which may be done numerically. However, we deal with this integral analytically, which requires some linear algebra manipulations, when K_y is constant. In the nonlinear case, we use-one step linearization, which works well, because the grid is adjusted to the local gradient in both the x and y directions. One can see that if the mesh is aligned with the magnetic field then the parallel flux does not contaminate the perpendicular flux due to the vanishing dx.

As already mentioned, the unknowns are cell-averaged. However, the 'natural' approximation of the integral of a sink R over the cell as a sum of the partial

https://doi.org/10.1017/S0022377899007679 Published online by Cambridge University Press

integrals over subtriangles as $\sum \int_{E_k} R\,dx\,dy \approx R(T_i) \sum S_k$ is inadequate owing to the high sensitivity of the numerical solution T_i to the $R(T)$. We integrate the sink in the following way.

(i) Two coefficients, a_x^k and b_x^k, for a three-point bilinear interpolation function

$$f_3^k(x, y) = T_{k_1} + a_x^k(x - x_{k_1}) + b_y^k(y - y_{k_1}) \tag{28}$$

are obtained for each of the triangular elements (which can always be done).

(ii) The integrals $\int_{E_k} R(f_3^k(x, y))\,dx\,dy$ are calculated either numerically by subdivision into smaller triangles, or (in some cases) analytically by local linearization of the radiation function, provided that $R(T)$ is differentiated numerically.

The set of implicit algebraic equations is solved either by using a direct solver for sparse matrices or by an iterative over-relaxation method. However, optimization of solvers, was not done, nor was comparison of the two methods. A typical run with 10^4 elements takes several minutes on a workstation. However, for the meshes with 10^5 vertices, the CPU time may easily exceed a few hours. To speed up calculations, we are envisioning the application of modern multigrid methods (Knoll et al. 1998).

The format of the unstructured mesh in the code is as follows: list of vertices, list of vertex connectivities, list of element connectivities, plus information on the alignment with the magnetic field (which side of the triangular element – if any – is parallel to the magnetic field). The format uses another important constraint, namely that the number of neighbouring elements is limited to three. This demand may be in conflict with the requirement for the alignment of the mesh with the field. One can see in Fig. 11 that the triangle at the beginning of a new magnetic surface is not aligned. We plan to remove the fixed number of neighbours constraint in the future.

As mentioned previously, the grid adaption in a two-dimensional domain is performed using the following quasi-one-dimensional procedure. The region is covered initially by a set of lines aligned with the magnetic field. These lines may be clearly seen in Figs 3(b) and 6, where the 'field' is respectively radial and vertical. Vertices are distributed along each of the lines using a one-dimensional algorithm described by Batishchev et al. (1998). The algorithm distributes the prescribed number of vertices, with spacings inversely proportional to the gradients, calculated along the line. The adaption to the cross-field gradients is performed in accordance with the following procedure: if the perpendicular gradient becomes locally high then a subline, which is also parallel to the magnetic field, is generated. The new line breaks if the gradient drops back. The quasi-one-dimensional procedure is then applied to each new subline, and the mesh is regenerated every time from the very beginning. The number of levels of subdivision is unlimited, but it rarely exceeds 10, which corresponds to a 1000-fold refinement of the initial grid.

The proposed approach to building two-dimensional unstructured adaptive grids is very efficient, because it is effectively reduced to a set of one-dimensional problems. Mesh refinement time is negligible compared with the solution time of the implicit system. As a side-benefit, it automatically gives us triangular elements with one side parallel to the field. This property was found to be vital to treat the large anisotropies of the cross- and along-field diffusivity coefficients.

https://doi.org/10.1017/S0022377899007679 Published online by Cambridge University Press

4. Grid-free approach

We have to admit that the price paid for adaptivity is high, because the grids become unstructured, time-varying and a challenge to manage. Fortunately, there are grid-free methods, which effectively deal with a 'cloud of vertices' with no mutual connectivity required. Local stencils are determined on-the-fly from the stability and accuracy conditions (see below). We study the applicability of one such method (Kholodov 1991) to edge-plasma problems. This approach constructs the difference scheme using a positive approximation for any second-order nonlinear elliptic equation. The method can deal with an arbitrarily shaped domain, bounded by any number of unconnected boundaries. The approach is based on the properties of the difference schemes in the space of undetermined coefficients for functions defined on a cloud of arbitrarily located vertices. It is characterized by the following features:

(i) it is ideal for complex geometries;

(ii) it is explicit;

(iii) it is unconditionally stable for time-dependent problems;

(iv) it is high-order accurate.

However, for non-linear problems it requires internal iterations.

For illustration, let us consider the second-order stationary quasilinear elliptic equation

$$V_{xx} + e_{12}V_{xy} + e_{22}V_{yy} + e_1V_x + e_2V_y = F(x, y, V), \tag{29}$$

$$e_{22} > \tfrac{1}{4}e_{12}^2, \qquad e_{ml} = e_{ml}(x, y, V), \qquad e_l = e_l(x, y, V), \qquad m, l = 1, 2, \tag{30}$$

with the Dirichlet boundary conditions

$$V_\Gamma = V^P(g), \tag{31}$$

where g is the distance along the boundary. Let us first introduce boundary vertices $r_i = (x_i, y_i), i = 1, \ldots, I$, and specify a grid function V_i, as given by (31). Next, let us place (arbitrary) K additional vertices inside the simulation domain: $r_k = (x_k, y_k), k = 1, \ldots, K$, and assign desired values V_k to each of them.

Now we assume that the stencil is not fixed, and for each inner point r_k we consider a linear difference expression

$$V_k = \sum_{j=j_1}^{j_J \geqslant 10} a_{kj}V_j - \beta_0 F_k - \beta_1 F_{xk} - \beta_2 F_{yk}, \tag{32}$$

which involves at least ten vertices. Here F_k, F_{xk} and F_{yk} are the right-hand side of (29) and its spatial derivatives at the kth vertex. They do not necessarily have to have consecutive subscripts. The boundary nodes may be included as well.

Next, we expand the difference expression (32) in a Taylor series in the vicinity of the pivot point r_k, and demand second-order accuracy of the approximation. This will require satisfaction of the following conditions:

$$\sum_j a_{kj} = 1, \tag{33}$$

$$\sum_j a_{kj}X_j\{1 - \tfrac{1}{2}X_j[e_1 - \tfrac{1}{3}X_j(e_1^2 + F_V - e_{1x}) + Y_j e_{1y}]\} = 0, \tag{34}$$

https://doi.org/10.1017/S0022377899007679 Published online by Cambridge University Press

$$\sum_j a_{kj}\left(Y_j - \tfrac{1}{2}X_j^2\{e_1 - X_j[e_1^2 + \tfrac{1}{3}X_j(e_2F_V - e_1e_2 + e_{2x}) + Y_j(F_V - e_{2y})]\}\right) = 0, \quad (35)$$

$$\sum_j a_{kj}X_j\{Y_j - \tfrac{1}{2}X_j[e_{12} + \tfrac{1}{3}X_j(e_2 - 2e_1e_{12} + e_{12x}) + Y_j(e_1 + e_{12y})]\} = 0 \quad (36)$$

$$\sum_j a_{kj}\{Y_j^2 - X_j^2[e_{22} - \tfrac{1}{3}X_j(e_{12}e_2 + e_1e_{22} - e_{22x}) + Y_j(e_2 + e_{22y})]\} = 0 \quad (37)$$

$$\sum_j a_{kj}X_j[3Y_j(Y_j - e_{12}X_j) - X_j^2(e_{22} - e_{12}^2)] = 0 \quad (38)$$

$$\sum_j a_{kj}[Y_j^3 - e_{22}X_j^2(3Y_j - e_{12}X_j)] = 0, \quad (39)$$

$$2\beta_0 = \sum_j \tfrac{1}{2}a_{kj}X_j^2(1 - \tfrac{1}{3}e_{11}X_j), \quad (40)$$

$$6\beta_1 = \sum_j a_{kj}X_j^3 \quad (41)$$

$$2\beta_2 = \sum_j a_{kj}X_j^2Y_j, \quad (42)$$

where we have used the notation $X_j = x_j - x_k$ and $Y_j = y_j - y_k$. Usually, the neighbours for each point can be chosen so that

$$a_{kj} \geqslant 0, \qquad j = j_1, \ldots, j_J, \qquad J \geqslant 10. \quad (43)$$

This condition guarantees that the finite-difference operator will be monotonic and positive-definite, which is known to be crucial for stability. The search for the neighbours is performed in each of the 20 sectors (see Fig. 13), to satisfy the conditions (33)–(42). In the nonlinear case, iterations, with possible refreshment of the neighbours, are required. We cannot prove that the system (33)–(42) is always solvable. However, our experience shows that we have always been able to solve it, even in nonlinear cases.

A first attempt has been made to apply this method to SOL plasma-related model problems. We illustrate the method's efficiency by solving two problems with diffusion dominance.

4.1. Model problem I

We consider a quasilinear heat conduction–radiation equation in a box geometry,

$$V_{xx} + C_y(x, y, V)V_{yy} = S(x, y, V), \qquad X \times Y \in L_x \times L_y \quad (44)$$

with the following boundary conditions: at $y = L_y$, the incoming heat flux $q_0(x)$ is fixed, while at the other boundaries, V is set equal to a small positive value. The contours of the calculated V for particular $C_y \gg 1$ and S are shown in Fig. 14. We note that the arrangement of vertices was regular, and their total number was about 1000.

4.2. Model problem II

We now consider the heat conduction equation in a domain with two unconnected boundaries. For illustration, we picked an Alcator C-Mod-like geometry. The boundary conditions were just two fixed temperatures: a hot core, T_C=100, and a cold edge, $T_E = 1$. The simulation domain is covered by a cloud of arbitrarily placed

https://doi.org/10.1017/S0022377899007679 Published online by Cambridge University Press

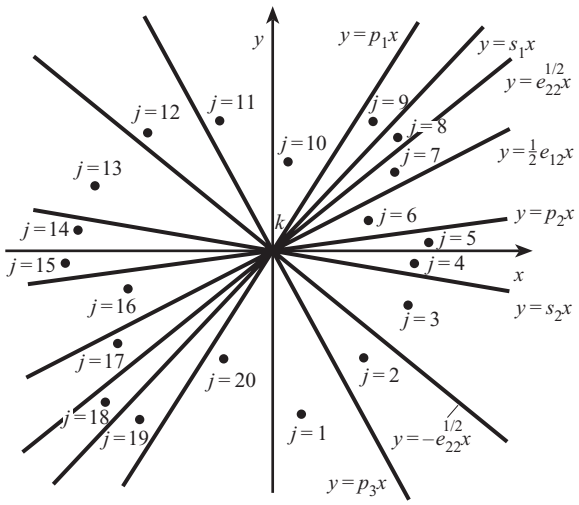


Figure 13. *k*th vertex neighbourhood is divided into 20 sectors to ensure the construction of the second-order monotonic difference scheme by the grid-free method.

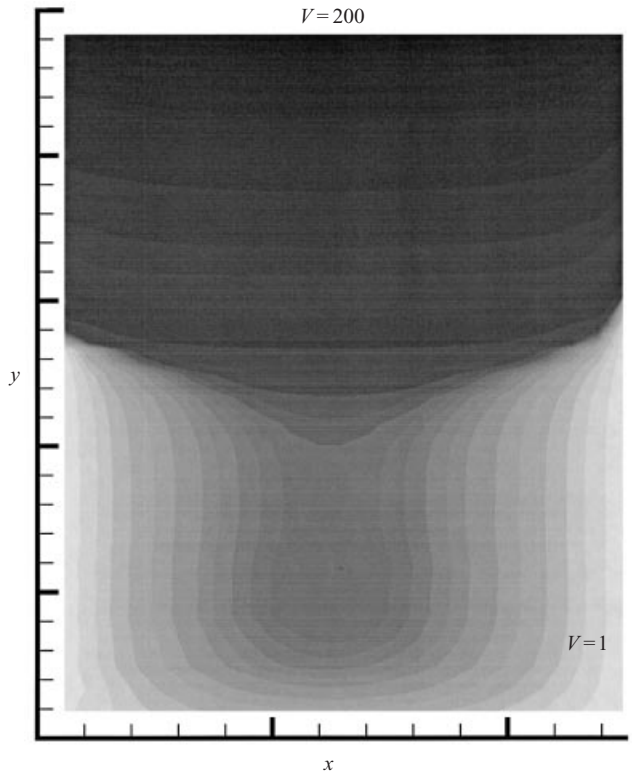


Figure 14. Contours of V as calculated for a second-order quasilinear equation in a box geometry.

https://doi.org/10.1017/S0022377899007679 Published online by Cambridge University Press

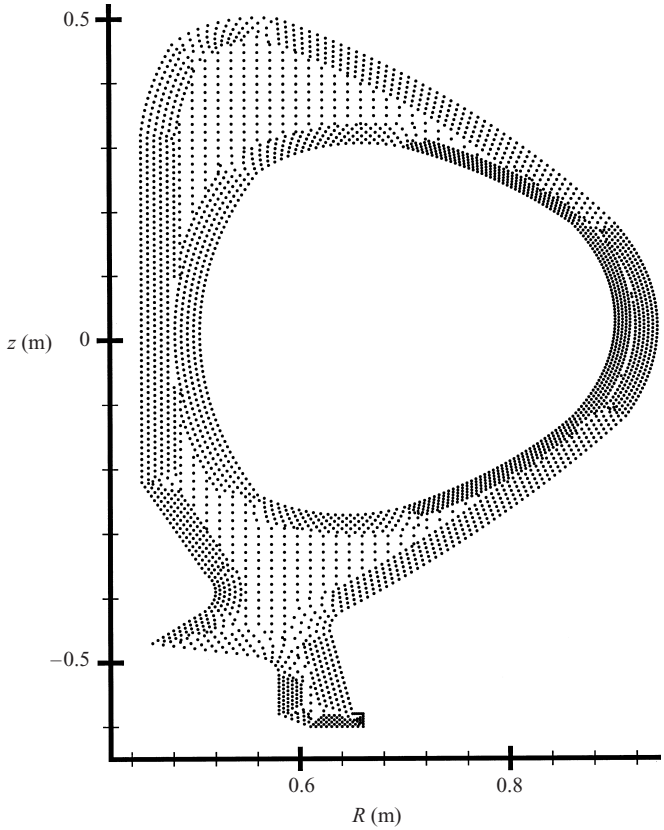


Figure 15. Cloud of arbitrarily placed vertices for the Alcator C-Mod geometry with two unconnected boundaries.

vertices (about 3000 in this run). Their spatial distribution is shown in Fig. 15. Figure 16 shows the numerical solution that was obtained using this cloud of vertices and the grid-free method.

We have not compared the accuracy of the model problems I and II results with other methods or with analytical solutions, since this would not be straightforward because of nonlinearities and the complex geometry. However, a test for a quasi-linear equation in a rectangular geometry with a known non-smooth analytical solution showed 10^{-5} relative accuracy, and it took about 200 iterations to achieve it.

5. Conclusions

(1) A new algorithm for the adjustment of an unstructured adaptive triangular grid is proposed. It allows one to build two-dimensional meshes very effectively using a quasi-one-dimensional approach. The grid is aligned with the magnetic field, while its variable resolution takes into account local plasma gradients in both directions. A new discretization scheme has been employed for edge-plasma applications. Our approach combines the flexibility of finite-elements methods and the conservative properties of finite-volume methods. The method

https://doi.org/10.1017/S0022377899007679 Published online by Cambridge University Press

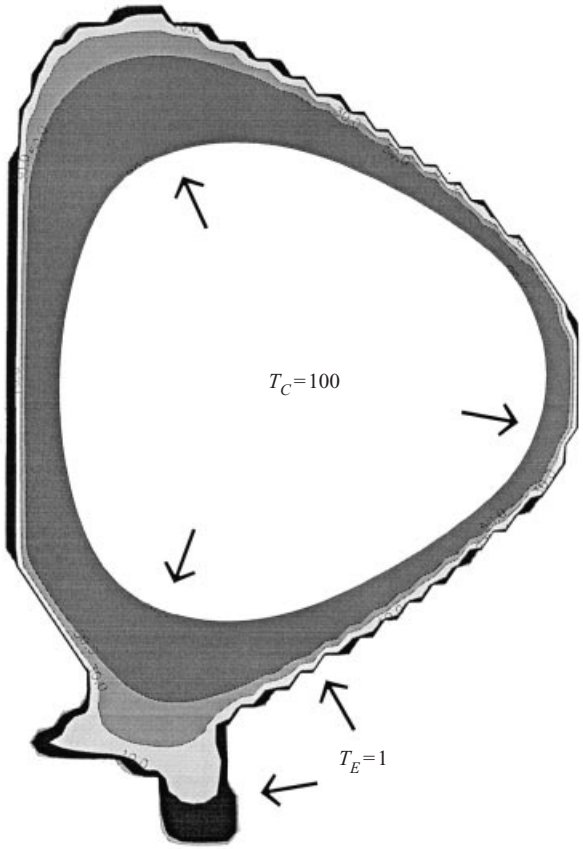


Figure 16. Contours of the temperature profile that was obtained by applying the grid-free method to the cloud of vertices shown in Fig. 15.

has been benchmarked on several nonlinear test problems with anisotropic coefficients, sharp fronts and bifurcated solutions. The total number of vertices required to achieve the same accuracy used with standard structured meshes is found to be almost two orders smaller.

(2) A fast and accurate grid-free method has been applied to scrape-off-layer plasma problems. The method is stable, and very flexible. It can easily simulate regions with complex geometry and with unconnected boundaries. It is not conservative, but is extremely efficient even for nonlinear cases. We suggest that it be used in conjunction with other implicit methods as a preconditioner in fluid codes.

(3) Exact analytical and semi-analytical solutions of the nonlinear diffusion–radiation equation with edge-plasma-related properties have been obtained. They may exhibit bifurcation of solutions and may contain sharp fronts and unconnected boundaries. The structure of these solutions is controllable via adjustable parameters. This makes them very useful for the benchmarking of various numerical methods and codes that are being developed for nonlinear plasma problems.

https://doi.org/10.1017/S0022377899007679 Published online by Cambridge University Press

Acknowledgements

This work was supported by US DOE Grants DE-FG02-97-ER-54392 at Lodestar Research Corporation and DE-FG02-91-ER-54109 at the MIT Plasma Science and Fusion Center. O.V.B. would like to acknowledge colleagues S. I. Krasheninnikov and D. J. Sigmar from the MIT PSFC Fusion Theory and Computations group.

References

Baliga, B. R. and Patankar, S. V. 1983 *Numer. Heat Transfer* **6**, 245.

Batishchev, O. V., Knoll, D., Rognlien, T., Krasheninnikov, S., Rensink, M. and Batishcheva, A. 1998 *Contrib. Plasma Phys.* **38**, 361.

Kholodov, A. S. 1991 *Math. Model.* **3**, 104 (in Russian).

Knoll, D. A., Lapenta, G. and Brackbill, J. U. 1998 In: *Proceedings of 16th International Conference on Numerical Simulation of Plasmas, Santa Barbara, CA, 10–12 February 1998*, p. 134.

Krasheninnikov, S. I. 1997 *Phys. Plasmas* **4**, 3741.

Marchand, R., Meo, F., Simard, M., Stansfield, B., Haddad, E., Abel, G., Lachambre, J. L., Pinsonneaut, D. and Richard, N. 1998 In: *Proceedings of 13th International Plasma Surface Interaction Conference, San Diego, CA, 18–22 May 1998*, p. 3P-27 (to be published in *J. Nucl. Mater.*).

Wising, F., Knoll, D. A., Krasheninnikov, S. I., Rognlien, T. D. and Sigmar, D. J. 1996 *Contrib. Plasma Phys.* **36**, 136.

Zanino, R. 1996 *Contrib. Plasma Phys.* **36**, 407.

Zanino, R. and Subba, F. 1998 *Contrib. Plasma Phys.* **38**, 355.

https://doi.org/10.1017/S0022377899007679 Published online by Cambridge University Press